

Submitted for inclusion in: Passive Microwave Remote Sensing Research Related to
Land-Atmosphere Interactions (B. Chandrasekhar, Y. Kerr,
E. Njoku, and P. Sampath, eds.)

SURFACE TEMPERATURE ESTIMATION OVER LAND USING SATELLITE
MICROWAVE (TMI) 10A4 ETRY

Eni G. Njoku

Jet Propulsion Laboratory
California Institute of Technology
Pasadena, CA 91109, USA

ABSTRACT

Surface temperature is an important parameter of the physical processes that govern the fluxes of energy and water at the biosphere-atmosphere interface. The energy and Water fluxes have major influences on the Earth's weather and climate. Models ranging from local to global scales are required to understand and predict effects of the energy and water fluxes. Satellite-derived land surface temperature measurements can be used to develop and calibrate these models, and to monitor long-term environmental changes. Infrared and microwave techniques have been applied successfully to the measurement of surface temperature over the oceans. The measurement of surface temperature over land using similar techniques has received less attention. This is due partly to the complexity of the electromagnetic interactions with the land surface and to the variability in land surface types. Microwave measurements are feasible under nearly all weather conditions (except for precipitation). This is an advantage in the tropics and desert regions where clouds, dust, and aerosols frequently obscure the surface at infrared wavelengths. This advantage is offset, for some applications, by the relatively low spatial resolution of microwave radiometers. The purpose of this paper is to review the status of microwave sensing of land surface temperature for bare and vegetation-covered soils, and to indicate current limitations in applications to global climate and environmental monitoring.

1.0 INTRODUCTION

The land surface temperature plays an important role in the Earth's surface energy balance and hydrologic cycle. Energy is provided to the Earth in the form of incident solar radiation, a portion of which is reflected and absorbed by the atmosphere, while the remainder reaches the surface. At the surface there is a balance between the net radiation flux (solar and longwave) entering the surface, the sensible and latent heat fluxes from the surface to the atmosphere, and the heat flux into the surface. These fluxes are influenced by surface characteristics such as soil type, soil moisture, and vegetation cover, and by atmospheric variables such as air temperature, humidity, windspeed, cloudiness, and precipitation.

Understanding the dynamics of the surface and atmospheric variables, their feedback effects, and human-induced changes, is critical for modeling and predicting climate and environmental change. Early simulations with climate models showed that reductions in soil moisture and vegetation cover could alter the regional balances of energy and water fluxes, leading to global patterns of decreased precipitation and increased surface temperature over land (Walker and Rountree [1]; Shukla and Mintz [2]). Recent simulations using more sophisticated models have shown similar results, e.g. Dickinson and Held-Sellers [3]. Chahine et al. [4] have used data from the High-resolution Infra-Red Sounder (HIRS) on the NOAA polar-orbiting satellites to produce monthly mean Global maps of surface skin temperature (defined as the top infrared radiating layer of the surface) illustrating the diurnal and seasonal global temperature changes. Such data may be used routinely to validate climate models. Studies by Carlson et al. [5] and Price [6] using data from the Heat Capacity Mapping Mission (HCMM), and by Klaassen and van den Berg [7], Taconet et al. [8], and others, using data from the Advanced Very High Resolution Radiometer (AVHRR) on the NOAA satellites, have shown that infrared-derived surface temperatures may be used with one-dimensional boundary layer models to derive surface fluxes of sensible and latent heat. Similarly, Wetzel and Woodward [9] have used data from the Visible-Infrared Spin-Scan Radiometer (VISSR) on the NOAA geostationary satellites to infer surface soil moisture. These studies have demonstrated the usefulness of satellite-derived surface temperature measurements for global monitoring and flux studies.

Satellites provide the only viable means for measuring land surface temperatures globally. Conventional (*in situ*) measurements of near-surface air temperature, such as

collected by the worldwide network of surface meteorological stations, are inadequate for these purposes since the spatial sampling and coverage are inadequate in many regions of the world. Furthermore, the near-surface air temperatures typically differ significantly (i.e. by more than a few degrees) from the ground and canopy surface temperatures that parameterize the surface energy balance models. Satellite measurements are better suited to providing data for these models since they measure the temperature of the ground surface, and provide area-averaged rather than point values. The main limitations in using satellite data are the need to correct for variable surface emissivity and atmospheric attenuation, and the difficulty in quantifying the temperature measurement accuracy due to the lack of comparable in situ data.

For the above reasons, increasing attention is being paid to the problem of retrieving accurate satellite measurements of land surface temperature (LST). Aspects of the infrared and microwave techniques have been studied by several investigators, e.g. Price [10], Wan and Dozier [11], Becker and Li [12], and McFarland et al. [13]. Most studies have addressed infrared techniques, primarily due to the higher spatial resolutions available from infrared sensors (- 1 km versus -- 10 to 100 km for microwave sensors), and also to the historical availability of data from satellite infrared sensors such as the ITCM, AVHRR, TM, and VISSR. Microwave measurements, however, are feasible under nearly all weather conditions (except for precipitation). This is an advantage in the tropics and deserts where clouds, dust, and aerosols frequently obscure the surface at infrared wavelengths. This advantage is offset, for some applications, by the relatively low spatial resolution of microwave radiometers. Long-term microwave data sets are available from the Scanning Multichannel Microwave Radiometer (SMMR) on the Nimbus-7 satellite and the Special Sensor Microwave Imager (SSM/I) on the DMSP satellites. The availability of these data sets, and the potential of continued data from the SSM/I series and future sensors such as the Multi-frequency Imaging Microwave Radiometer (MIMR) on the Earth Observing System (EOS), has renewed interest in the potential of microwave measurements of LST for climate monitoring and model development and validation.

In this paper the status of satellite microwave measurements and retrieval techniques for LST are reviewed. In the first part of the paper the surface energy balance is discussed briefly as a means for understanding the role of surface temperature in the fluxes of energy and water at the land surface. This is followed by a discussion of the theoretical basis for microwave measurement of LST. In subsequent sections some results

of satellite microwave observations are discussed, and simple model simulations and regression techniques are used to examine the potential for multichannel microwave surface temperature estimation.

2.0 BACKGROUND

Surface fluxes (in particular evapotranspiration) have major influences on weather and climate. Thus, it is essential to understand the physical processes that govern these fluxes, and, in particular, to represent the processes of evaporation and transpiration realistically in the climate models. Evaporative cooling is a major determinant of the land surface temperature, and depends not only on the precipitation input to the surface, and how this is apportioned into evaporation, soil storage, and runoff, but also on how the net radiative energy is divided between latent and sensible heat fluxes. The surface energy balance determines the relationships between these fluxes.

The surface energy balance equation may be expressed in the form

$$R_n = H + LE + G \quad (1)$$

where R_n is the net radiation into the surface, H is the sensible heat flux from the surface to the atmosphere, LE is the latent heat flux into the atmosphere, and G is the flux of heat into the soil. The latent heat flux, LE , is the product of the latent heat of evaporation, L , and the evaporation rate, E . For conceptually simple surfaces, straightforward expressions can be derived for the energy balance components. These are:

$$R_n = R_{S1} (1 - A) + R_{L1} - \varepsilon \sigma T_s^4 \quad (2)$$

$$H = \rho C_p (T_s - T_a) / r_a \quad (3)$$

$$E = \rho [q_s(T_s) \cdot q_a] / (r_c + r_a) \quad (4)$$

$$G = -\lambda \frac{\partial T}{\partial z} \quad (5)$$

In Equation (2), $R_{S\downarrow}$ is the incident solar energy at the surface, Λ is the surface albedo, $R_{L\downarrow}$ is the incident thermal infrared energy (minus any reflected), ε is the surface emissivity, σ is the Stefan-Boltzman constant, and T_s is the surface temperature. For the sensible heat flux, T_s and T_a are the surface temperature and the near-surface air temperature, respectively, C_p and ρ are the specific heat and density of air, respectively, and r_a is a 'resistance' coefficient. For the evaporation, q_a is the water vapor mixing ratio of the near-surface air and q_s is the saturation water vapor mixing ratio of the surface. The canopy resistance, r_c , is zero for bare soil. Note that q_s is a function of the surface temperature, T_s . For the soil heat flux, λ is the thermal conductivity and T is the soil temperature as a function of depth z . In climate models the soil heat flux is of minor significance and is usually ignored. The above expressions are discussed in more detail elsewhere (e.g. Dickinson et al. [14]).

Equations (1) through (5) illustrate the role of LST in affecting both the energy and the moisture fluxes at the surface. For natural surfaces, which may include mixtures of bare soil, vegetation canopy of different types, and undergrowth, Equations (2)-(5) can be modified to take into account the radiative transfer and fluxes within the canopy (e.g. Sellers et al. [15]; Taconet et al. [8]). A unique definition of surface temperature is difficult in this case since different temperatures are involved in the equations. These include the soil surface temperature, the soil near-surface temperature, the temperature of the air within the canopy, the temperature of the leaf surfaces of the canopy, and the internal leaf tissue temperature. In remote sensing, the surface temperature is normally defined as a weighted mean temperature over the radiating ('skin' or 'penetration') depth in the medium. The penetration depth depends on the electromagnetic attenuation in the medium, and, for microwaves, is a function primarily of the moisture content of the medium and the radiation wavelength. In microwave sensing, this depth may vary from a millimeter or less in moist soils at short wavelengths, to over a meter in sparse vegetation or dry soil at long wavelengths. Furthermore, spaceborne sensor antenna footprints, of spatial dimensions 10 to 100 km, may encompass a variety of canopy types and soils. Thus, the satellite brightness temperatures often represent a rather complicated weighted mean temperature over the surface radiating volume within the footprint. These considerations show that care must be taken in relating the surface temperature measured by a satellite radiometer to the appropriate surface temperature parameters of surface flux and climate models.

3.0 THEORETICAL BASIS

3.1 *Surface 'Effective' Temperature*

The microwave radiation received by a spaceborne radiometer viewing land may be expressed approximately as

$$T_{bp} = T_u + \exp(-\tau_a)[T_{bp} + r_p T_d] \quad (6)$$

where T_{bp} is the surface brightness temperature, T_u and T_d are the upwelling and downwelling atmospheric radiation components, τ_a is the atmospheric opacity, r_p is the surface reflectivity, and T_{bp} is the brightness temperature received at the radiometer. The subscript p refers to polarization which may be $p = h$ (horizontal) or $p = v$ (vertical). The dependence on incidence angle θ is understood. If we assume that the subsurface dielectric properties are horizontally homogeneous and vary slowly with depth the surface brightness temperature can be written in approximate radiative transfer form

$$T_{bp} = e_p T_e \quad (7)$$

where $e_p = (1 - r_p)$ is the surface emissivity, and T_e is the 'effective' (or 'skin') temperature of the surface given by

$$T_e = \int_{-\infty}^0 T(z) \alpha(z) \exp\left[-\int_z^0 \alpha(z') dz'\right] dz \quad (8)$$

The integration is performed for radiation emanating from all depths up to the surface. The attenuation coefficient in the medium, $\alpha(z)$, depends on the dielectric constant, and, for nadir viewing, can be expressed simply as $\alpha(z) = 4\pi n''(z)/\lambda$, where $n''(z)$ is the imaginary part of the refractive index of the medium, and λ is the wavelength. (For a medium whose dielectric constant profile varies rapidly over the distance of a wavelength in the medium, the more accurate coherent model formulation must be used in place of the radiative transfer equation (Njoku and Kong [16]).)

The effective temperature is a weighted mean of the vertical temperature profile in the medium, and may differ substantially from the actual surface temperature. Examples of weighting functions for a bare soil are shown in Figure 1 (Njoku and Kong [16]), where

the weighting function is defined as the factor multiplying $T(z)$ in the integrand of Equation (8). The weighting functions shown, Γ_N , have been normalized to a maximum value of unity, for ease of comparison, since their absolute magnitudes include the effects of surface emissivity. Weighting functions at shorter wavelengths (higher frequencies) sample the temperature close to the surface, whereas at longer wavelengths the weighting functions show that the radiation originates from deeper in the medium, and the effective temperature is therefore characteristic of the weighted mean temperature over a greater depth. Note that for dry surface conditions with a positive moisture gradient the weighting functions may not peak at the surface. For a medium of uniform dielectric constant (e.g. uniform soil moisture profile) the weighting functions are exponentials, and are characterized by the penetration depth, $d = \lambda/4\pi n^2$, at which the weighting functions decrease to 1/e of their value at the surface. Figure 2 shows a plot of the penetration depth versus wavelength in sandy soil, for various moisture contents. At 1.5 GHz the penetration depth varies from approximately 10 cm to 1 m for soil conditions ranging from saturated to dry, while at 30 GHz the penetration depth varies from less than 1 mm to a little over 1 cm for similar conditions.

Choudhury et al. [17] have computed the differences between the surface temperature and the effective temperature for a range of naturally occurring soil moisture and temperature profiles. Figure 3 shows scatterplots of effective temperature versus surface temperature for these profiles. At 10.7 GHz, ($\lambda = 2.8$ cm), the effective temperature agrees with the surface temperature to within a few degrees centigrade over the diurnal temperature cycle. However, at 1.4 GHz, ($\lambda = 21$ cm), the effective temperature differs by as much as 15 to 20 °C near mid-day from the surface temperature for these semi-arid zone profiles. Choudhury et al. [17] suggest that the effective temperature can be related empirically to the surface temperature, T_s , and the temperature at large (infinite) depth, T_∞ , by the expression

$$T_e = T_\infty + (T_s - T_\infty) C \quad (9)$$

where C is a least-squares-fitted parameter that depends on wavelength and to a lesser degree on soil type. For a given location and soil type, if T_∞ and C can be computed or estimated, then T_s may be determined from satellite-derived estimates of T_e .

When the surface is covered by vegetation, similar considerations apply, except that the weighting functions and penetration depth depend on the attenuation coefficient of

the vegetation volume, which in turn depends on the vegetation biomass (density and water content). In the following discussions, we shall refer to T_e as the surface temperature, for simplicity, with the understanding that the effective temperature is implied.

3.2 Atmosphere and Emissivity Effects

The atmospheric emission contributions to the received radiation may be expressed approximately as $T_u \approx T_d \approx T_a[1 - \exp(-\tau_a)]$, where T_a is a weighted mean temperature over the absorbing region in the atmosphere (lower troposphere) that varies with wavelength. Values for T_a are typically between 10 and 20 °C lower than the surface air temperature at atmospheric window frequencies. Using these approximations, Equations (6) and (7) lead to the expression

$$T_{bp} = T_a [1 - \exp(-\tau_a)] - r_p \exp(-\tau_a) + c_p T_e \exp(-\tau_a) \quad (10)$$

At frequencies below approximately 10 GHz, the opacity, τ_a , is usually less than 0.03 for non-precipitating conditions, and the first term in Equation (10) is small. The observed brightness temperature, T_{bp} , is then approximately equal to the surface brightness temperature, T_{bp} , given by Equation (7). At higher frequencies, and especially for the 37 and 85 GHz channels of the SMMR and SSM/I instruments, the atmospheric contributions cannot be safely ignored, and Equation (10) is a more accurate representation. Figure 4 shows the opacity as a function of frequency at $\theta = 50^\circ$ incidence angle (typical of the SMMR and SSM/I sensors), for an annual tropical, cloud-free atmosphere with 0 to 5 g/cm² integrated water vapor.

The effects of surface temperature, emissivity, and atmospheric opacity on brightness temperature, computed by Equation (10), are shown in Figure 5. The expected increases of brightness temperature with increasing emissivity and surface temperature are observed. From Figure 5(b) we note that increasing atmospheric opacity increases the brightness temperature at low emissivities, since the atmospheric temperature (T_a) is higher than the surface brightness temperature ($T_{bp} = c_p T_e$). Conversely, the brightness temperature decreases with opacity at high emissivities ($c_p \approx 1$). The crossover point depends on the difference between the surface and atmospheric temperatures ($T_e - T_a$).

3.3 Surface Temperature Error Sensitivities

Equation (10) may be rearranged to express the surface temperature in terms of the emissivity, atmospheric variables, and the observed brightness temperature

$$T_e = \{T_{Bp} - T_a[1 - \exp(-\tau_a)][1 + (1 - e_p)\exp(-\tau_a)]\} / \{e_p \exp(-\tau_a)\} \quad (11)$$

If the atmospheric variables, T_a and τ_a , and the surface emissivity, e_p , are known or can be estimated, then the surface temperature, T_e , may be obtained from single-channel measurements of the observed brightness, T_{Bp} . In practice, the variability in τ_a may be small (at low frequencies) or may be estimated from coincident radiosonde measurements. In some cases the variability in e_p may also be estimated from knowledge of the surface type and moisture content. To investigate the accuracies with which e_p , τ_a , T_a , and T_{Bp} must be known to obtain a reliable estimate of T_e , one may study the partial derivatives of Equation (11), i.e. the sensitivities of T_e to the observed or estimated quantities

$$\frac{\partial T_e}{\partial e_p} = -\exp(\tau_a)[T_{Bp} - 1 - (1 - \exp(-w)) / e_p^2] \quad (12)$$

$$\frac{\partial T_e}{\partial \tau_a} = \exp(\tau_a) \{T_{Bp} - T_a[1 + (1 - e_p)\exp(-2^*0)]\} / e_p \quad (13)$$

$$\frac{\partial T_e}{\partial T_a} = -\exp(\tau_a)[1 - e_p \exp(-\tau_a) - (1 - e_p) \exp(-27)] / e_p \quad (14)$$

$$\frac{\partial T_e}{\partial T_{Bp}} = \exp(\tau_a) / e_p \quad (15)$$

The functional forms of these derivatives are plotted in Figure 6 for representative ranges of values. Figures 6(a) and G(b) show that to obtain an accuracy of 3°C in T_e the emissivity must be known to an accuracy of between 0.006 and 0.012, depending on the values of T_e and e_p . This corresponds to an accuracy of approximately 1%, since one may

assume approximate values of $T_e = 300$ K and $e_p = 0.8$, and, for small τ_a , $\frac{\Delta T_e}{T} \approx \frac{\Delta e_p}{e_p}$.

Such accuracy in a-priori knowledge of emissivity appears unrealistic given the natural variability of 10 to 25% or greater found for e_p in many regions. On the other hand, surface classification schemes (e.g. Townshend et al. [18] and Neale et al. [19]) can be used to identify the gross surface type. Within each surface type the emissivity is influenced

primarily by moisture. The use of multiple channels may permit the moisture, and thereby the emissivity, to be estimated sufficiently accurately to retrieve the surface temperature. This procedure may be carried out using multiple regression or iterative retrieval methods as discussed in the next section.

At frequencies less than 10 GHz where the variability in atmospheric opacity is small ($\Delta\tau_a < 0.01$), Figures 6(c) and (d) show that the effect of uncertainties in opacity on T_e will also be small. At higher frequencies this may not be the case. For example, with reference to Figure 4, a radiosonde-derived water vapor measurement uncertainty of 0.1 g/cm² leads to uncertainties of approximately 0.003 and 0.02 in opacity at 37 and 85 GHz, respectively, with corresponding errors in T_e of 0.3 and 2 °C for an emissivity of 0.8. The presence of clouds will further increase the errors. These errors decrease as the emissivity increases. For low opacities, Figure 6(e) shows that the effect on T_e of uncertainties in T_a is small. Finally, Figure 6(f) shows that radiometer noise will be amplified in the estimation of T_e , typically by a factor of between 1 and 2, with higher values occurring in regions of low emissivity and high opacity.

4.0 MULTICHANNEL RETRIEVALS

The magnitudes of the corrections necessary to account for effects of variable surface emissivity and atmospheric opacity when estimating surface temperature were discussed in the previous section. These corrections may be attempted using independent water vapor (radio sonde) and cloud measurements, and a-priori emissivity estimates, or alternatively they may be made by using multichannel data such as available from the SMMR and SSM/I, or a combination of both approaches may be used. There has been limited research in studying these approaches however.

4.1 *Satellite Retrievals*

Few studies of surface temperature using satellite microwave data have been reported in the literature. One study is that of McFarland et al. [13] who investigated the rms errors resulting from multiple linear regressions of SSM/I data against air temperatures measured at surface meteorological stations across the U.S. Great Plains. The air temperatures were obtained from the NOAA operational climatological database and represent measurements at screen height (1.2 m). By using SSM/I data from

ascending (morning) overpasses occurring between 0600 and 0700 local solar time, and comparing these with the minimum air temperatures reported for the same morning from the meteorological stations, an attempt was made to minimize the differences between the ground surface temperature and the screen height air temperature. For the range of temperatures encountered (1.1 to 26.7 °C), the authors report possible rms errors as high as 2.85 °C in using point-located minimum air temperatures in this manner as comparisons for the footprint-average SSM/I data at the exact time of overpass. The regressions between surface air temperatures, T_{as} , and SSM/I brightness temperatures, T_{Bt} , can be expressed as

$$T_{as} = a_0 + \sum_{i=1}^N a_i T_{Bi} \quad (16)$$

where a_i are regression coefficients, and N is the number of channels used in the regressions. Figure 7 shows the results of these regressions for the surface type classified as 'moist soil', displayed as the predicted temperature from Equation (16) versus the actual values of screen air temperature. The channels selected in the regression, 85V, 37V, 22V, and 19H, have the coefficients tabulated in the figure. Also shown is the rms error of the regression, and similar statistics for the other land surface types within the study region. For moist soil, the magnitude of the coefficients indicates that the surface temperature is most highly correlated with the 85V channel, while the remaining channels provide information to correct, for emissivity and atmospheric variability. This is reasonable since the 85 GHz radiation originates close to the surface, and for vertical polarization the 53° incidence angle of SSM/I is close to the Brewster angle, thereby reducing the variability due to surface emissivity for this channel. For dry soils, however, 22V appears to be the most significant channel, indicating perhaps that what is being sensed is the lower atmosphere rather than the surface.

From these results a number of observations can be made. First, the rms errors of the regression fits appear promising since they are in the range 2 - 2.6 °C over a dynamic range of 4 - 23 °C, and the correlation coefficients in some cases are above 0.8. However, the rms errors mask a variety of error sources as mentioned earlier. The regression coefficients have been tuned to the conditions of the specific study region and hence the equations cannot be applied reliably to other regions. The variability of the coefficients from one surface type to another also indicates that surface classification errors may lead to corresponding surface temperature errors.

4.2 Model Simulations

The problem may be analyzed from another perspective by performing simulations using a simple radiative transfer model. In this model, vegetation is represented as an absorbing layer above the soil, characterized by an opacity τ_c , with soil reflectivity r_{sp} . If the soil surface and vegetation are assumed to be at the same temperature, Kerr and Njoku [20] have shown that Equation (10) describes the brightness temperature viewing this two-layer medium if r_s is replaced by $r_{sp} \exp(-2\tau_c)$. i.e. Equation (10) is replaced by

$$T_{Rp} : T_a [1 - \exp(-7)][1 + r_{sp} \exp(-\tau_a - 2\tau_c)] + T_e \exp(-\tau_a)[1 - r_{sp} \exp(-2\tau_c)] \quad (17)$$

The canopy opacity can be expressed as

$$\tau_c = A \frac{\epsilon_{sw}}{\lambda} W / \cos \theta \quad (18)$$

where W is the vegetation water content, ϵ_{sw} " is the imaginary part of the dielectric constant of the vegetation water, λ is the wavelength, θ is the incidence angle, and A is a coefficient that depends on vegetation type. The soil reflectivity depends on surface roughness and on soil dielectric constant which can be related to the soil moisture, m_v , using data given by Hallikainen et al. [21] and Njoku and Kong [16]. The atmospheric opacity can be related directly to the atmospheric integrated water vapor, ρ_v (Waters [22]). These relationships are discussed more fully in Kerr and Njoku [20].

Equation (17) allows the satellite-observed brightness temperature to be computed as a function of a limited number of atmospheric and surface parameters, i.e. $T_{Rp} = f(\rho_v, T_e, m_v, W)$. A simulated data set can then be generated by computing T_{Rp} using Equation (17) for various combinations of parameter values chosen to cover a suitable dynamic range. This was done for values covering the ranges: $\rho_v = 0.5$ to 5.0 g/cm^2 ; $T_e = 4$ to 40°C ; $m_v = 0.03$ to 0.3 g/cm^3 ; and $W = 0$ to 0.2 kg/m^2 . Ten values were selected to cover the ranges in equal increments for each parameter, and brightness temperatures were computed for all possible combinations of each parameter value, for a total of 10^4 combinations. For each combination, ten brightness temperatures were computed at frequencies of 6.6, 10.7, 18, 21, and 37 GHz, vertical and horizontal polarizations, and 50° incidence angle, to simulate measurements of the Nimbus-7 SMMR satellite instrument. The SMMR frequencies are also of interest since they correspond closely to the frequencies that will be used for the

future EOS Multifrequency Imaging Microwave Radiometer (M IMR) instrument (ESA [X]); frequencies higher than 37 GHz were not computed since the assumption in Equations (17) and (18) of vegetation as an absorbing (non-scattering) layer is not valid at the higher frequencies. (Strictly speaking the validity is in question at frequencies greater than about 10 GHz, but the error is not expected to be too great up to 37 GHz).

The simulated data set was used to develop a regression algorithm for surface temperature of a form similar to Equation (1) (i), i.e.

$$T_e = a_0 + \sum_{i=1}^N a_i F_i(T_B) \quad (19)$$

where T_B is a vector of the ten brightness temperatures. The F_i are functions of the ten brightness temperatures, and allow for regressions on functions of the brightness temperatures as well as on the brightness temperatures themselves. This helps mitigate some of the nonlinearities in the model Equation (17). Examples of such functions are $F_i = 1/1.1 (315/T_{Bj})$ and $F_i = (T_{Bj} \cdot T_{Bk})/(T_{Bj} + T_{Bk})$, to account for exponential nonlinearities, in the first case, and to investigate the use of functions that are independent of surface temperature, in the second. Regression techniques for microwave radiometry have been discussed elsewhere (Hofer and Njoku [24]). Caution must be used in interpreting rms errors of regressions on nonlinear functions since the errors will in general not be normally distributed.

Application of the regression formula of Equation (19) to the simulated data set gave the results shown in Figure 8. A stepwise regression procedure was used in which the single brightness temperature channel, T_{Bj} , (or function of channels, F_i) was first selected that was most highly correlated to the surface temperature. Additional channels (or functions) were then selected for the regression in successive steps, such that the residual error was minimized at each step for the L selection. The stepwise procedure was terminated when the addition of further channels to the regression did not reduce the residual error significantly from the previous step. This led to the following equation

$$T_e^* = a_0 + a_1 \ln(315 \cdot T_{B37V}) + a_2 \left(\frac{T_{B10V} \cdot T_{B10H}}{T_{B10V} + T_{B10H}} \right) + a_3 T_{B37V} + a_4 \ln(315 \cdot T_{18H}) \quad (20)$$

The rms residual error between the predicted temperature, T_e^* , from Equation (20) and the actual temperature, T_e , was 2.07 °C. This simulation did not take into account the effects of

radiometer noise in the brightness temperatures which would increase the rms residual error slightly. If only brightness temperatures, and not nonlinear functions, were used in the regressions, then the residual rms error increases to 2.9 °C. This value seems to be significantly larger than observed in Figure 7. However, the dynamic range of surface temperature used for the simulations was much larger, and no attempt was made to classify the simulations into groupings of dry, wet, and low vegetated soils.

The intent of the regression simulations is to show that the results obtained using satellite data are consistent with model simulation results. Limitations of the non-scattering vegetation model preclude analysis of the suitability of the 85 GHz channel for surface temperature measurement, but the selection of the higher frequency channels in the simulation regressions results directly from the fact that the higher frequencies are less sensitive to surface emissivity variability (in the simulations the 37V channel showed the highest correlation to surface temperature). Due to the nonlinearity of the problem, it is likely that, iterative or neural network methods would be more appropriate for developing a useful surface temperature retrieval algorithm.

5. CONCLUSIONS

Surface temperature has a major effect on land surface microwave emission and can be estimated from satellite measurements of brightness temperature if the natural variability in surface emissivity and atmospheric opacity can be accounted for. Multichannel measurements are one method of estimating and correcting for the emissivity and atmospheric effects. Limited satellite data analyses and theoretical simulations have shown that surface temperature estimation accuracies of 2 to 2.5 °C should be feasible using a nonlinear retrieval algorithm. The accuracy may be improved if a priori information on the surface emissivity is available. Additional research and data analysis are required to investigate these approaches. It is difficult to assess the accuracy of satellite-derived temperature estimates since comparable in situ data are generally unavailable over spatial scales typical of the satellite footprints. If satellite temperature measurements are used in energy balance models care should be taken in defining the effective temperature consistently in the models and radiative transfer formulations. Since several years of global satellite data are now available from the SMMR and SSM/I instruments, a concerted effort should be made to develop surface

temperature products from these data to compare with GCM model output and to examine regions] seasonal and interannual temperature variability .

6. ACKNOWLEDGMENT

This work represents one phase of research carried out at the Jet Propulsion Laboratory, California Institute of Technology, under contract with the National Aeronautics and Space Administration.

7. REFERENCES

- [1] J. Walker and J. R. Rowntree, "The effect of soil moisture on circulation and rainfall in a tropical model," Quart. J. Roy. Met. Soc., Vol. 103, pp. 29-46, 1977.
- [2] J. Shukla and Y. Mintz, "Influence of land-surface evapotranspiration on the Earth's climate," Science, Vol. 215, pp. 1498-1500, 1982.
- [3] R. E. Dickinson and A. Lebel-Sellers, "Modelling tropical deforestation: A study of GCM land surface parameterizations," Quart. J. Roy. Met. Soc., Vol 114, pp. 439-462, 1988.
- 141 M. T. Chahine, R. Haskins, J. Susskind, and D. Reuter, "Remote sensing of land-surface temperature from the HIRS/MSU data," Proc. IISCP Conference, Rome, Italy, ESA SP-248, 1986.
- [5] T. N. Carlson, J. K. Dodd, S. G. Benjamin, and J. N. Cooper, "Satellite estimation of the surface energy balance, moisture availability, and thermal indices," J. Appl. Meteorol., Vol. 20, pp. 67-87, 1981,
- [6] J. C. Price, "On the use of satellite data to infer surface fluxes at meteorological scales," J. Appl. Met. coro],, Vol. 21, pp.1111-1122, 1982.

- [7] W. Klaassen and W. vanden Berg, "Evapotranspiration derived from satellite observed surface temperatures," *J. Clim. and Appl. Meteorol.*, Vol. 24, pp. 412-424, 1985.
- [8] O. Taconet, R. Bernard, and D. Vidal-Madjar, "Evapotranspiration over an agricultural region using a surface flux/temperature model based on NC-AVHRR data," *J. Clim. and Appl. Meteorol.*, Vol. 25, pp. 284-307, 1986.
- [9] P. J. Wetzel and R. H. Woodward, "Soil moisture estimation using GOES-VISSR infrared data: A case study with a simple statistical method," *J. Clim. and Appl. Meteorol.*, Vol. 26, pp. 107-117, 1987.
- [10] J. C. Rice, "Land surface temperature measurements from the split window channels of the NOAA-7 Advanced Very High Resolution Radiometer," *J. Geophys. Res.*, Vol. 89, pp. 7231-7237, 1984.
- [11] Z. Wan and J. Dozier, "Infrared-surface temperature measurement from space: Physical principles and inverse modeling," *IEEE Trans. Geosci. Rem. Sens.*, Vol. 27, pp. 268-278, 1989.
- [12] F. Becker and Z.-L. Li, "Towards a local split window method over land surfaces," *Int. J. Rem. Sens.*, Vol. 11, pp. 369-393, 1990.
- [13] M. J. McFarland, R. L. Miller, and C. M. U. Neale, "Land surface temperature derived from the SSM/I passive microwave brightness temperatures," *IEEE Trans. Geosci. Rem. Sens.*, Vol. 28, pp. 839-845, 1990.
- [14] R. E. Dickinson, A. Henderson-Sellers, C. Rosenzweig, and P. J. Sellers, "Evapotranspiration models with canopy resistance for use in climate models: A review," *Agric. and Forest Meteorol.*, Vol. 54, pp. 373-388, 1991.
- [15] P. J. Sellers, Y. Mintz, Y. C. Sud, and A. Dalcher, "A simple biosphere model (SiB) for use within general circulation models," *J. Atmos. Sci.*, Vol. 43, pp. 505-531, 1986.
- [16] E. G. Njoku and J. A. Kong, "Theory for passive microwave remote sensing of near-surface soil moisture," *J. Geophys. Res.*, Vol. 82, pp. 3108-3118, 1977.

- [17] B. J. Choudhury, T. J. Schmugge, and 'J'. Mo, "A parameterization of effective soil temperature for microwave emission," *J. Geophys. Res.*, Vol. **87**, pp.1 **301-1304**, 1982.
- [18] J. R. G. Townsend, C.O. Justice, B. J. Choudhury, C. J. Tucker, V. 'I'. Kalb, and 'I'. E. Goff, "A comparison of SMMR and AV111{1{ data for continental land cover characterization," *Int. J. Rem. Sens.*, Vol. 10, pp. **1633-1642**, 1989.
- [19] C. M. U. Neale, M. J. McFarland, and K. Chang, "Land-surface-type classification using microwave brightness temperatures from the Special Sensor Microwave/ Imager," *IEEE Trans. Geosci. Rem. Sens.*, Vol. **28**, pp.829-838, 1990.
- 1201 Y. 11. Kerr and E.G.Njoku, "A semiempirical model for interpreting microwave emission from semiarid land surfaces as seen from space," *IEEE Trans. Geosci. Rem. Sens.*, **vol. 28**, pp. **384-393**, **1990**.
- [211] M. 'J'. Hallikainen, F. 'I', Ulaby, M. C. Dobson, M. A. El-Rayes, and L.K. Wu, "Microwave dielectric behaviour of wet soil - Part 1: Empirical models and experimental observations, " *IEEE Trans. Geosci. Rem. Sens.*, Vol. **GE-23**, pp. 25-34, 1985.
- [221] J. W. Waters, "Absorption and mission by atmospheric gases," in: *Methods of Experimental Physics*, Vol. 12, Part B, (M. I., Meeks, Ed.). New York: Academic Press, 1976.
- [23] ESA, "The Multifrequency Imaging Microwave Radiometer," Instrument Panel Report, Publication No. ESA S1'-1 138, European Space Agency, Paris,1990.
- [24] R. Hofer and E. G. Njoku, "Regression techniques for oceanographic parameter retrieval using spaceborne microwave radiometry," *IEEE Trans. Geosci. Rem. Sens.*, vol. **GE-19**, pp. 178-189, 1981.

FIGURE CAPTIONS

- Figure 1. (a) Soil moisture profiles corresponding to (1) wet, and (2) dry conditions.
(b) Normalized temperature weighting functions, F_N , for moisture profile (1). (c) Normalized temperature weighting functions, F_N , for moisture profile (2). (Njoku and Kong [16]).
- Figure 2. Penetration depth as a function of wavelength for sandy soil with uniform moisture content between 1 and 30% by volume.
- Figure 3. Representative soil profiles of (a) moisture, and (b) temperature, for Phoenix, Arizona soil. Curves are labeled by number of days after irrigation. (c) Scatter plots of effective temperature versus surface temperature computed for profiles shown in (a) and (b) at various wavelengths. (Choudhury et al.[1 71]).
- Figure 4. Atmospheric opacity as a function of frequency in the range 1-100 GHz, for a cloud-free annual tropical atmosphere viewed at an incidence angle of 50°. Curves are for integrated water contents, ρ_v , of 0, 1, 2, and 5 g/cm².
- Figure 5. Brightness temperature dependence on: (a) surface temperature, T_e ; (b) surface emissivity, e_p ; and (c) atmospheric opacity, τ_a ; computed from Equation (10) with $T_a = 280$ K,
- Figure 6. (a) and (b): Sensitivity of estimated surface temperature, T_e , to surface emissivity, e_p , as a function of surface temperature and emissivity, respectively. (c) and (d): Sensitivity of estimated surface temperature, T_e , to atmospheric opacity, τ_a , as a function of surface temperature and emissivity, respectively. (e) and (f): Sensitivity of estimated surface temperature, T_e , to atmospheric temperature, T_a , and brightness temperature, T_{bb} , respectively, as functions of emissivity.
- Figure 7. Regression fit of 'predicted temperature' (linear combination of brightness temperature channels) to screen air temperature, for moist soils, covering central U.S. study region described by McFarland et al. [131]. Statistics for

other surface types are also shown. Brightness temperature data are from the DMSP SSM/I satellite instrument.

Figure 8. Comparison between actual, T_e , and estimated, T_e^* , surface temperature using multiple regression on a simulated brightness temperature data set. The dashed line is the perfect agreement line. An rms residual error of **2.07 °C was obtained**. However, due to the nonlinearity of the model, the errors are not normally distributed.

Figure 1

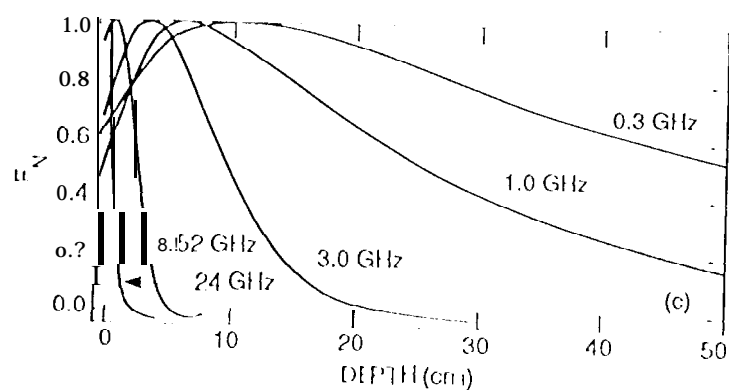
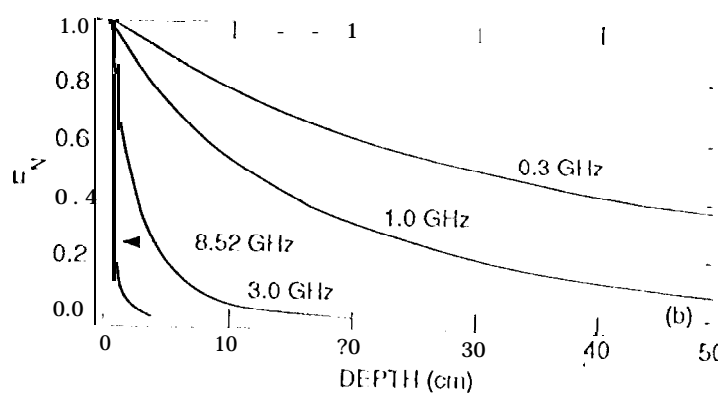
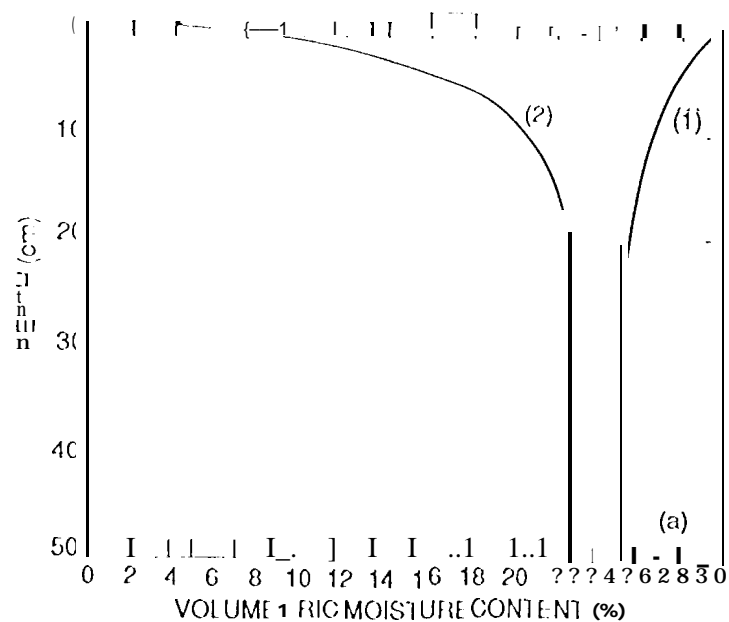


Figure 2

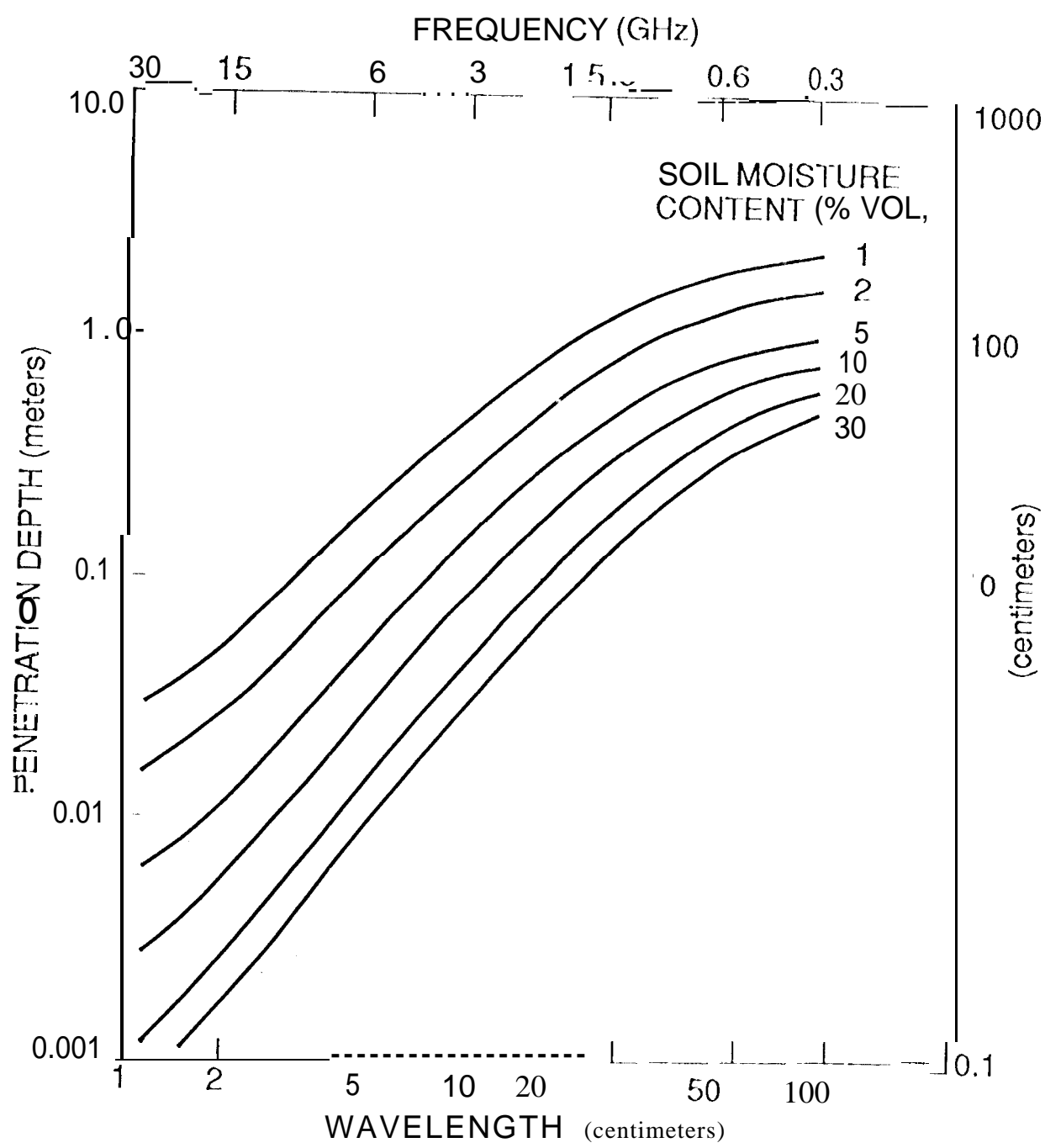


Figure 3

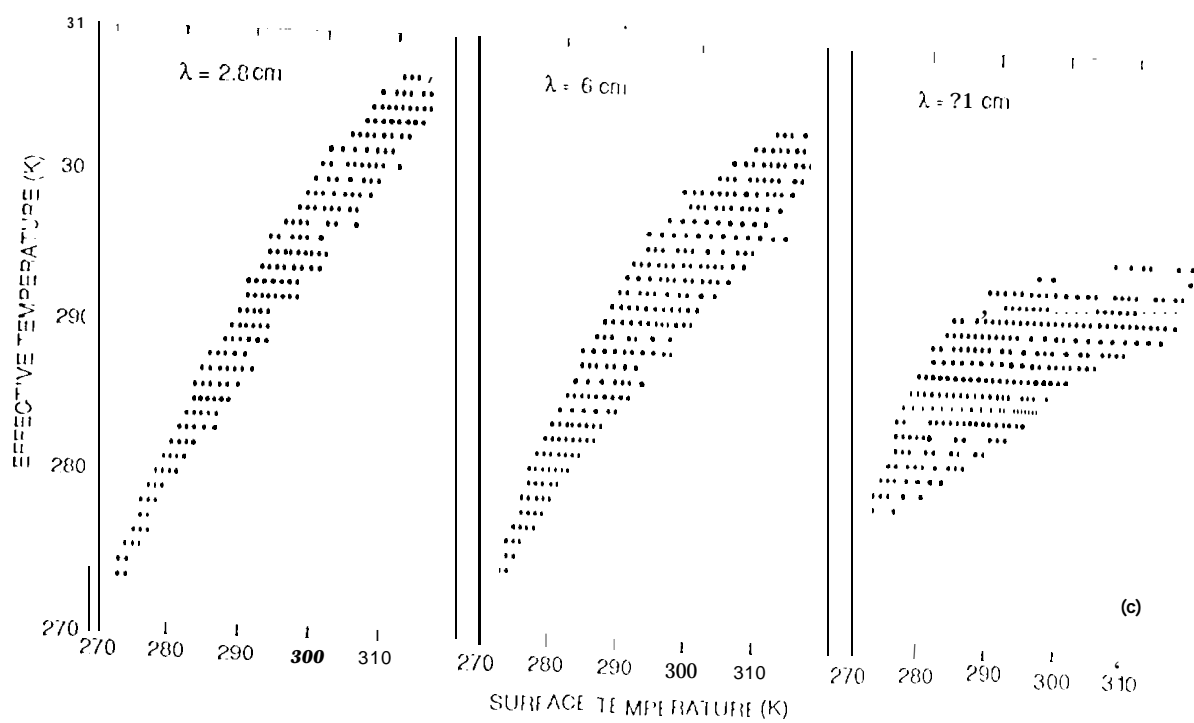
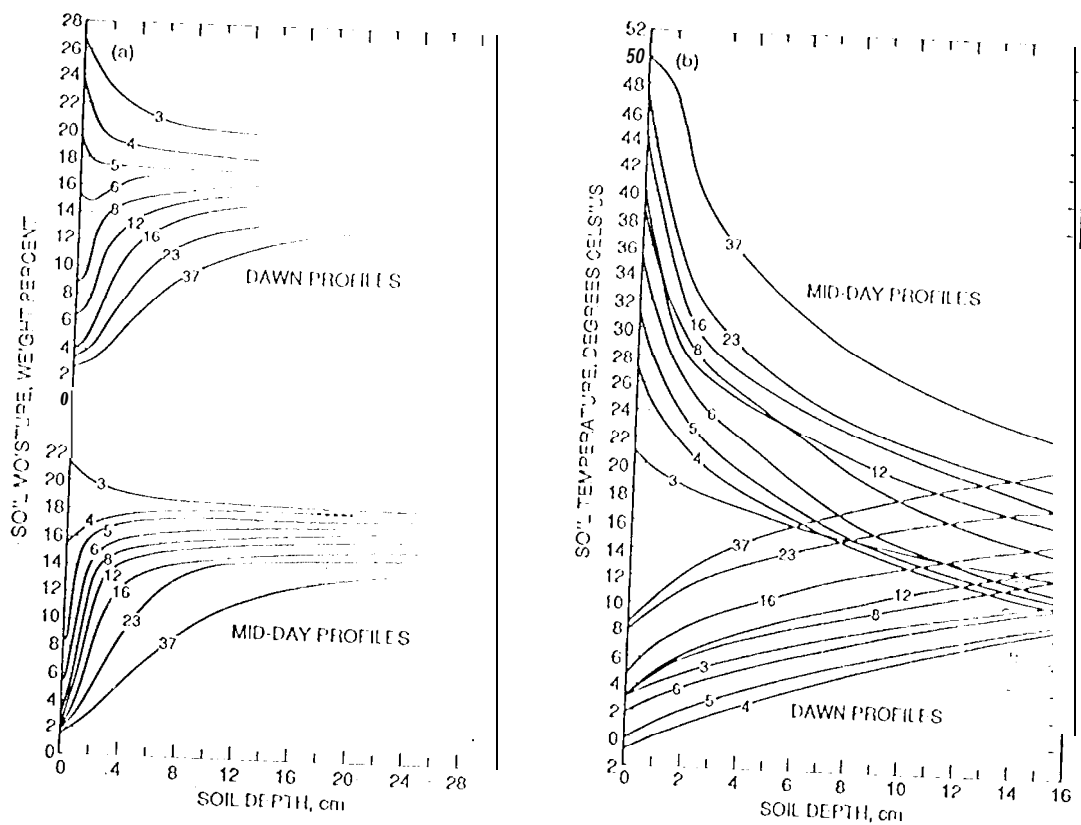


Figure 4.

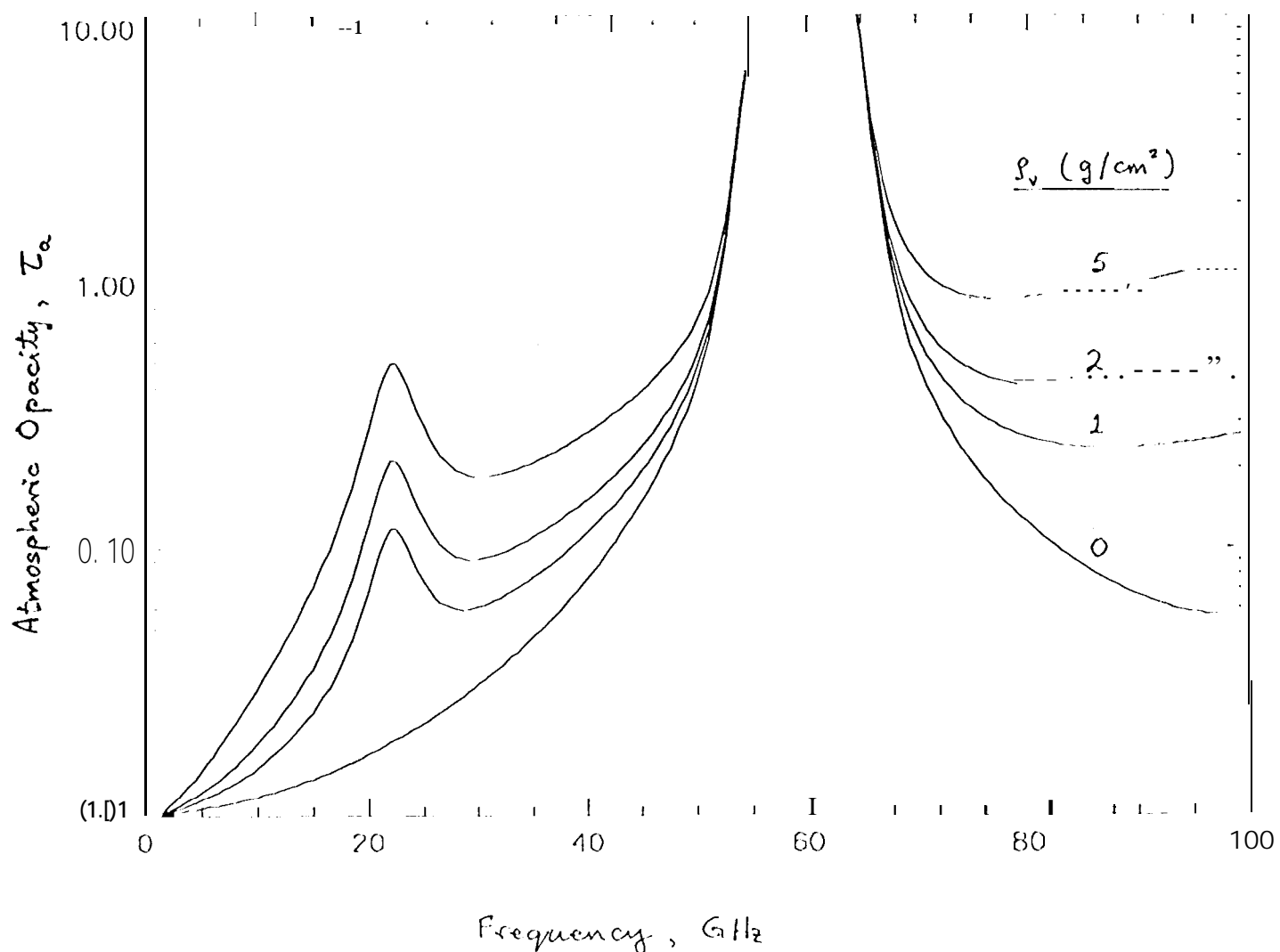


Figure 5

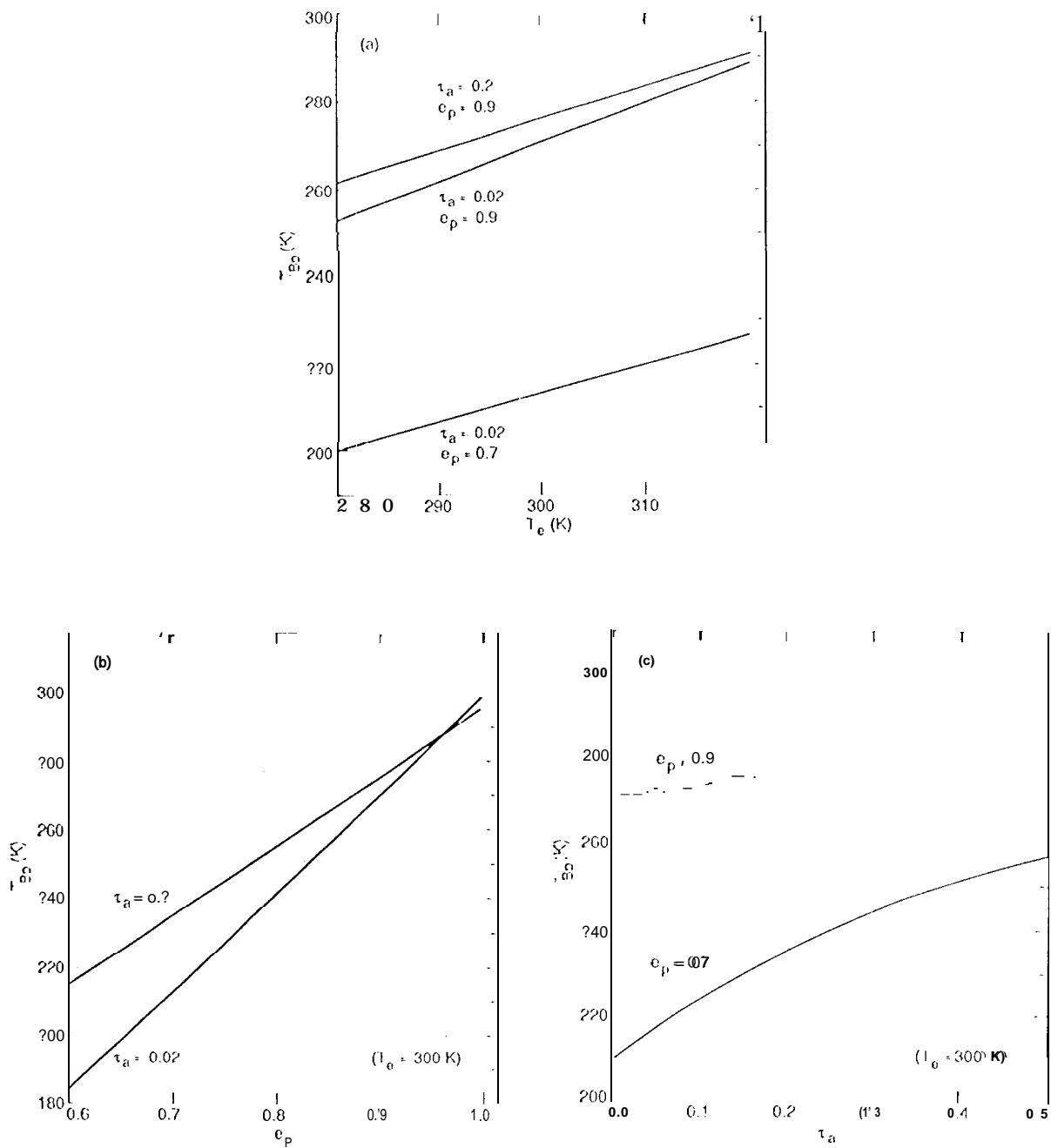


Figure 6

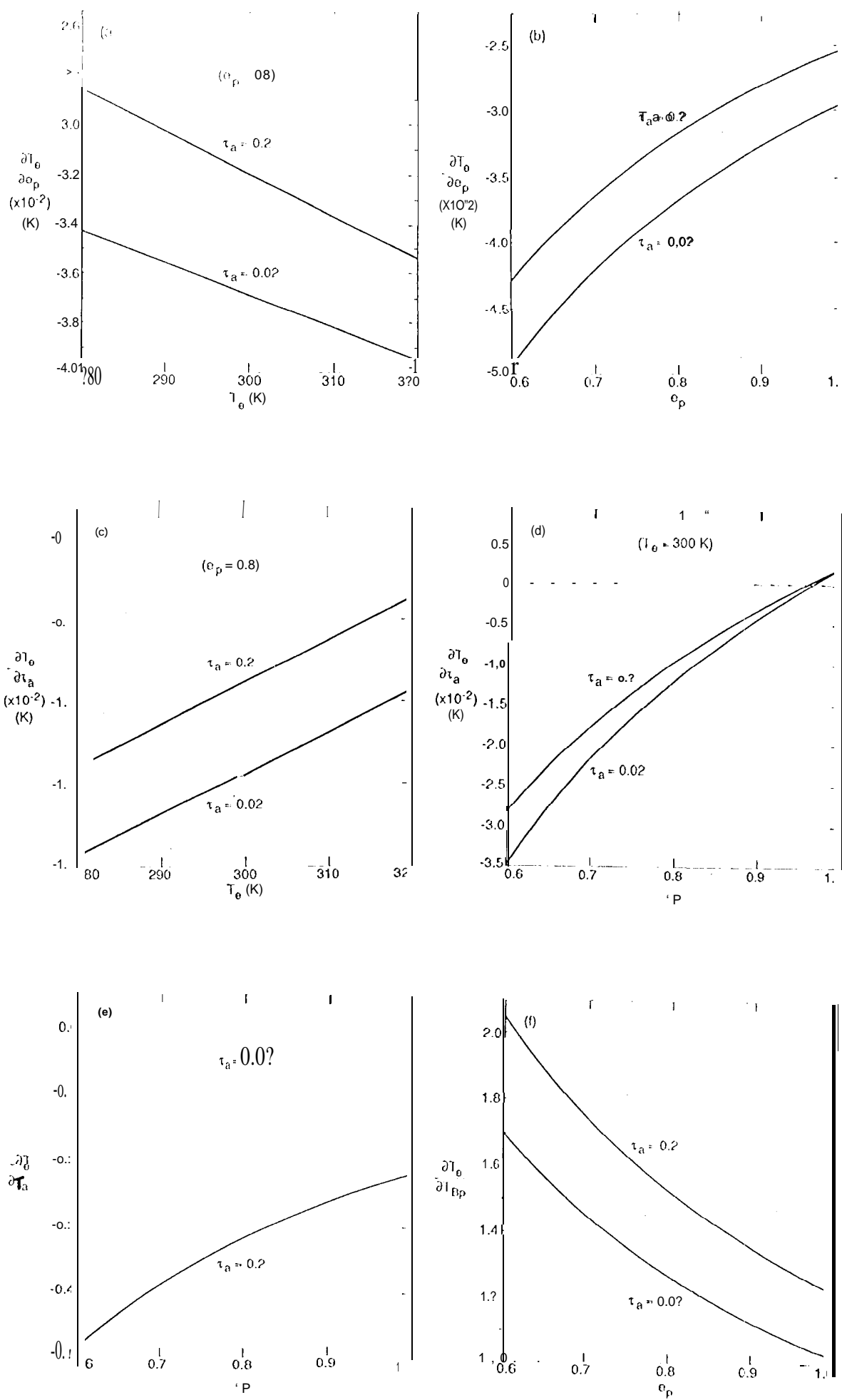
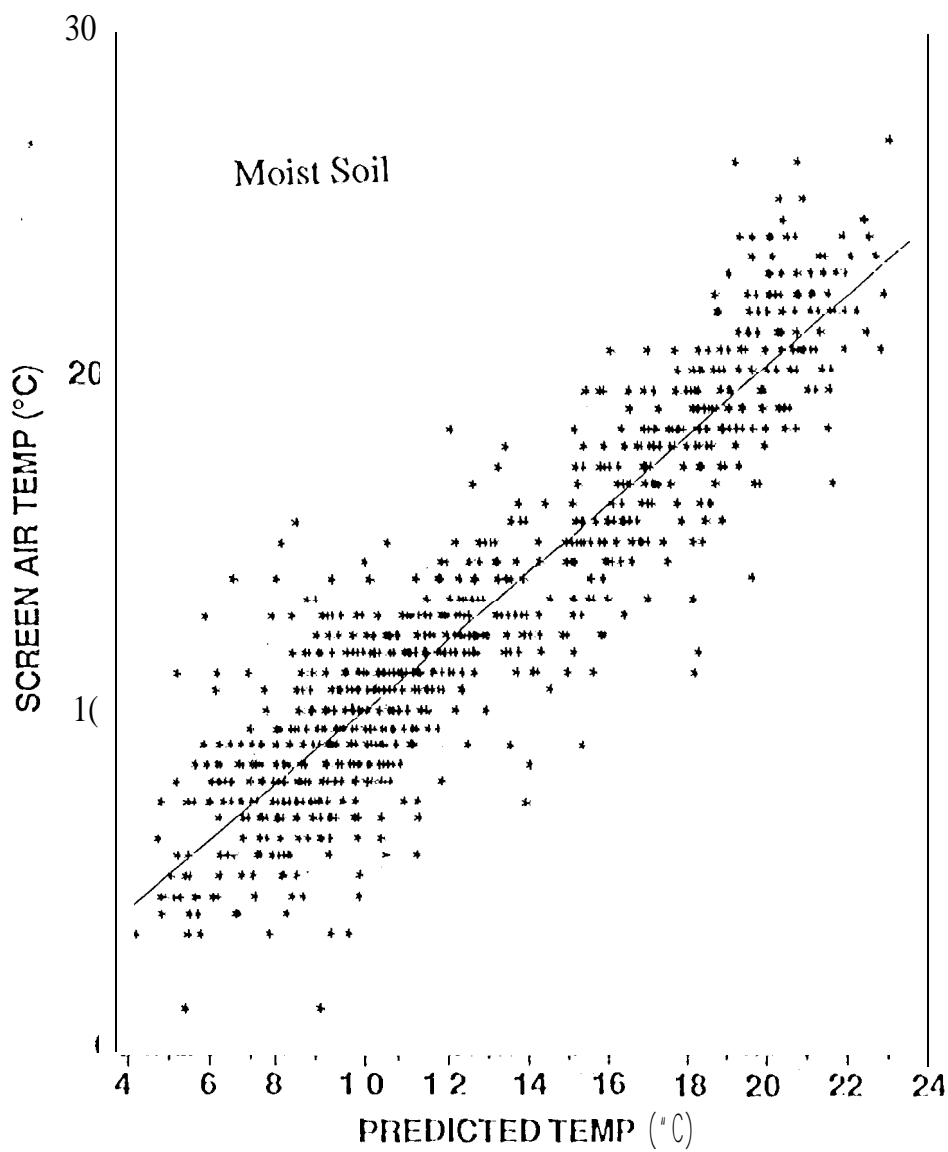


Figure 7



Regression Coefficients and Statistics for 4-Channel Model:

Land Surface Type	R ²	RMSE	Intercept	85.V	37.V	22.V	19.H
Crops/range	0.81	2.58	22.40	1.239	-0.396	0.275	-0.174
Moist soils	0.85	1.99	41.69	1.745	-0.724	0.415	-0.063
Dry soils	0.62	2.60	76.28	-0.367	-0.318	1.408	0.025
All	0.79	2.37	58.07	0.811	-0.555	0.730	-0.170

Figure 8

